nature nanotechnology

Article

https://doi.org/10.1038/s41565-024-01775-2

Construction of topological quantum magnets from atomic spins on surfaces

Received: 28 March 2024

Accepted: 26 July 2024

Published online: 29 August 2024

Check for updates

Hao Wang[1,2,4], Peng Fan[1,2,4], Jing Chen[1,2,4], Lili Jiang[2], Hong-Jun Gao[1,2], Jose L. Lado[3] ✉ & Kai Yang[1,2] ✉

Artificial quantum systems have emerged as platforms to realize topological matter in a well-controlled manner. So far, experiments have mostly explored non-interacting topological states, and the realization of many-body topological phases in solid-state platforms with atomic resolution has remained challenging. Here we construct topological quantum Heisenberg spin lattices by assembling spin chains and two-dimensional spin arrays from spin-1/2 Ti atoms on an insulating MgO film in a scanning tunnelling microscope. We engineer both topological and trivial phases of the quantum spin model and thereby realize first- and second-order topological quantum magnets. We probe the many-body excitations of the quantum magnets by single-atom electron spin resonance with an energy resolution better than 100 neV. Making use of the atomically localized magnetic field of the scanning tunnelling microscope tip, we visualize various many-body topological bound modes including topological edge states, topological defects and higher-order corner modes. Our results provide a bottom-up approach for the simulation of exotic quantum many-body phases of interacting spins.

The exploration of topological properties in condensed matter systems has sparked a paradigm shift in our comprehension of quantum phenomena, promoted for their potential for protected quantum information processing[1–7]. In the past few years, quantum simulations of non-interacting topological states have witnessed great progress[6,8–13]. Recently, advancements in experimental techniques have enabled the realization of interacting topological matter in a well-controlled manner[3–5]. For example, the many-body Su–Schrieffer–Heeger (SSH) model has been studied in precision-placed donors in silicon[3] as well as using Rydberg atoms[4].

Scanning tunnelling microscopes (STMs) can be used to fabricate precisely engineered topological matter at the atomic scale in a solid-state environment[14], such as single-particle SSH dimer chains[6] and electronic higher-order topological insulators[8], where the charge degrees of freedom are employed and these topological states can be understood by non-interacting models. By contrast, interacting spin systems constructed on surfaces[13,15–19] could potentially host many-body topological phases, but it remains a formidable task to fabricate and sense topological quantum magnets with atomic precision. Progress on atomic-precise topological spin systems was achieved only very recently. For instance, effective spin-1 Haldane chains composed of coupled spin-1/2 radicals were built using organic molecules on Au(111), where the end states are Kondo-screened by the metal substrate[7,20]. While previous studies have focused on one-dimensional (1D) topological spin chains on metals, topological spin chains or two-dimensional (2D) spin arrays have never been fabricated on a decoupling layer that protects the spins from screening, despite its vital importance in demonstrating their intrinsic topological behaviour—mostly owing to the challenge of precisely engineering magnetic interactions between atoms on insulators to reproduce the required spin Hamiltonian.

Here, we constructed topological quantum spin lattices with many-body topological modes including 1D dimerized spin chains and a 2D dimerized spin array with spin-1/2 Ti atoms on MgO in a

[1]Beijing National Laboratory for Condensed Matter Physics and Institute of Physics, Chinese Academy of Sciences, Beijing, China. [2]School of Physical Sciences, University of Chinese Academy of Sciences, Beijing, China. [3]Department of Applied Physics, Aalto University, Espoo, Finland. [4]These authors contributed equally: Hao Wang, Peng Fan, Jing Chen. ✉e-mail: jose.lado@aalto.fi; kaiyang@iphy.ac.cn

https://doi.org/10.1038/s41565-024-01775-2

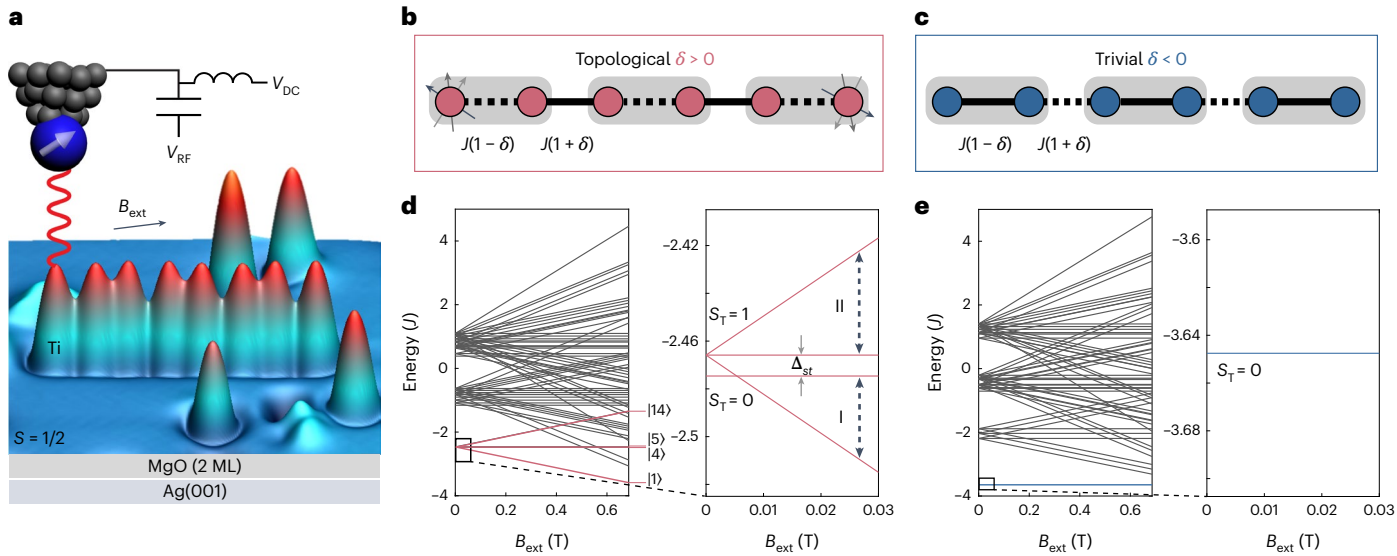

Fig. 1 | Realization of dimerized antiferromagnetic spin-1/2 lattices on a surface. a, Experimental setup showing an STM with ESR capability, and an STM image of Ti atoms on MgO/Ag(001). A spin-polarized tip is used to drive and sense ESR. **b**,**c**, Dimerized spin-1/2 chains with alternating antiferromagnetic coupling strengths $J(1-\delta)$ and $J(1+\delta)$, showing the topological ($\delta > 0$, **b**) and trivial configurations ($\delta < 0$, **c**). The grey rectangles indicate the chosen unit cells. **d**,**e**, Calculated energy level diagrams of 6-spin chains as a function of B_{ext} for the topological (**d**) and trivial (**e**) phases. Δ_{st} is the singlet–triplet splitting, and ESR transitions I and II are labelled. The topological phase exhibits nearly fourfold degenerate singlet and triplet ground states, while the trivial phase exhibits a singlet ground state.

low-temperature STM (Fig. 1). By tuning the antiferromagnetic exchange interaction, both topological and trivial phases are realized (Fig. 1b,c). Combining electron spin resonance (ESR) with STM, we measured their many-body spin transitions atom by atom with an ultrahigh energy resolution below 100 neV, and visualized the topological edge states and topological defects in the spin chains, as well as the higher-order corner modes in the 2D spin array. The ESR spectra also reveal the effective couplings between the topological modes, highlighting their many-body nature. Our quantum many-body calculations show that the interacting many-body topological states are resilient to Hamiltonian perturbations such as long-range and anisotropic couplings, providing a step beyond single-particle topology realized in non-interacting SSH models. This robustness arises from the protection provided by time-reversal symmetry to the many-body topological modes.

Note that the dimerized spin-1/2 chains have recently also been realized using nanographenes on a metal surface and the topological edge states are probed as Kondo resonances[21]. The use of MgO decoupling layer in our work improves the coherence time of the topological modes and allows us to demonstrate their intrinsic properties.

The spin lattices were made by positioning Ti spins on the two-monolayer (ML) MgO film on Ag(001) (refs. 19,22,23). For both adsorption sites of Ti on MgO, the Ti atom has spin $S = 1/2$ with no single-ion magnetocrystalline anisotropy. Two Ti spins couple via antiferromagnetic exchange interaction at close distances (<1 nm), as revealed by single-atom ESR[22,23]. The exchange coupling constant J shows exponential dependence on the separation r between Ti atoms, as described by an exponential function, $J = J_0 \exp(-r/d)$. For two bridge-site Ti atoms, $J_0 \approx 5.87 \times 10^4$ GHz and $d \approx 0.94$ Å (refs. 19,23). We fabricated spin lattices using bridge-site Ti atoms in the following.

1D topological quantum magnet

We first focus on the 1D topological spin model, which is realized via an engineered dimerization in a spin-1/2 chain. Their quantum states under external applied magnetic field B_{ext} (almost in-plane) are described by the following spin Hamiltonian[24]:

$$H = J(1-\delta)\sum_{n}^{L/2}\mathbf{S}_{2n-1}\cdot\mathbf{S}_{2n} + J(1+\delta)\sum_{n}^{L/2-1}\mathbf{S}_{2n}\cdot\mathbf{S}_{2n+1} + \sum_{n}^{L} g\mu_B\mathbf{B}_{ext}\cdot\mathbf{S}_n + g\mu_B\mathbf{B}_{tip}\cdot\mathbf{S}_m, \quad (1)$$

where $\mathbf{S}_n = (S_n^x, S_n^y, S_n^z)$ is the spin operator for site n and the total number of sites is L. The exchange coupling J is 15.5 GHz and dimerization constant δ is about 0.61 for the spin chains constructed, corresponding to 3 × 0 and 2.5 × 0.5 lattice constants of MgO. The g factor is about 1.8, and μ_B is the Bohr magneton[23]. Since the exchange coupling is exponential in distance, second-nearest-neighbour coupling can be neglected. The direction of the external field B_{ext} is defined as z in the following. The atomic-scale tip magnetic field B_{tip} is used both to drive ESR transitions and to tune the many-body spin states by exerting an exchange bias only on the spin S_m under the tip[25]. The unit cells of the dimerized chains are chosen by containing two weakly or strongly coupled spins, and the edges of the chains are then engineered to match the choice of the unit cell, respectively (Fig. 1b,c).

This quantum many-body generalization of SSH model based on interacting spin-1/2 features topological edge modes[24,26,27] (Supplementary Section 1). Despite being predicted theoretically long ago, the dimerized spin-1/2 Heisenberg chains have not been experimentally realized in artificial quantum systems. Here, we constructed dimerized spin-1/2 Heisenberg chains on MgO, and the many-body topological edge modes can be probed using a weak external magnetic field as shown below. In sufficiently long chains, the dimerized Heisenberg model exhibits a ground state with a fourfold degeneracy when $\delta > 0$, and this ground state comprises a singlet and a triplet state, originating from the dangling edge excitations (Fig. 1d)[28].

Topological edge modes of 6- and 8-spin chains

To realize these topological spin edge states, we first built a 6-spin chain in the topological configuration ($\delta > 0$) with alternating nearest-neighbour coupling of 6 and 25 GHz (Fig. 2a). When B_{ext} is applied, each spin multiplet with a total spin S_T fans out into its $2S_T + 1$ components, as expected for Heisenberg spin Hamiltonian. When

https://doi.org/10.1038/s41565-024-01775-2

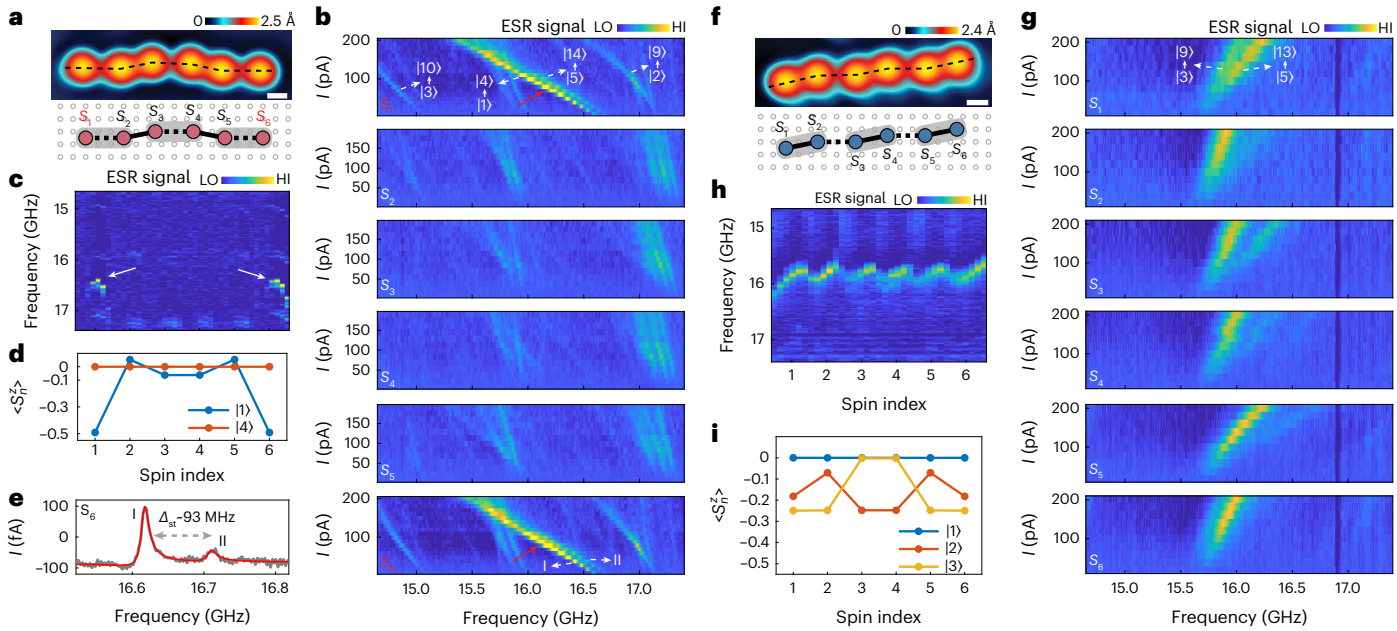

Fig. 2 | Topological versus trivial configurations of 6-spin chains. a, STM image (1.8 nm × 6 nm) and binding sites for the topological configuration (grey circles are oxygen sites of MgO). Scale bar, 5 Å. **b**, ESR spectra measured on each of the six spins as a function of setpoint current I, which is approximately proportional to B_{tip} (V_{DC} = 50 mV, I = 10–200 pA, V_{RF} = 5–28 mV, B_{ext} = 0.68 T). The red arrows indicate the edge modes. The initial and final states of ESR transitions are labelled. In the colour bar, LO and HI mean the lowest and highest ESR signals. **c**, ESR spectra measured along the dashed line in **a** (V_{DC} = 50 mV, I = 50 pA, V_{RF} = 16 mV). The white arrows indicate the edge modes. **d**, Calculated average magnetization $\langle S_n^z \rangle$ of the topological configuration for its ground state $|1\rangle$ and excited state $|4\rangle$. **e**, ESR spectrum showing transitions I and II, the frequency difference of which gives the singlet–triplet splitting (V_{DC} = 50 mV, I = 8 pA, V_{RF} = 28 mV). The red curve is a fit to a sum of asymmetric Lorentzian peaks. **f**, STM image (1.7 nm × 5.5 nm) and binding sites for a trivial configuration. Scale bar, 5 Å. **g**, ESR spectra measured on each of the six spins (V_{DC} = 50 mV, I = 20–200 pA, V_{RF} = 16–36 mV, B_{ext} = 0.61 T). The initial and final states of ESR transitions are labelled. **h**, ESR spectra measured along the dashed line in **f** (V_{DC} = 50 mV, I = 100 pA, V_{RF} = 28 mV). **i**, Calculated $\langle S_n^z \rangle$ of the trivial configuration for its ground state $|1\rangle$ and excited states $|2\rangle$, $|3\rangle$. Note that the opposite frequency shifts of the ESR peaks in **b** and **g** are due to opposite spin polarization of the particular STM tips used for measurement in each case.

B_{ext} = 0, the two lowest multiplets are one spin singlet and one spin triplet, resulting from the effective exchange coupling between the two edge states (Fig. 1d). With increasing B_{ext}, the triplet state aligned with the field becomes the ground state.

We investigated the eigenstates of this 6-spin chain by measuring ESR on different atoms and monitoring how the ESR spectra changed with the setpoint current I, which is approximately proportional to B_{tip} (Fig. 2b)[19,22]. The distinct responses of different ESR transitions to increasing B_{tip} enable us to clearly identify the initial and final states, as supported by our simulations (Supplementary Section 2)[19]. This method also reveals detailed information about the spin wavefunction and spin polarization at different sites[19]. The ESR peaks as indicated by red arrows in Fig. 2b reveal the transition from the ground state $|1\rangle$ to the excited state $|4\rangle$, which is the transition between the low-energy spin triplet ($|1\rangle = |S_T = 1, m_z = -1\rangle$) and singlet ($|4\rangle = |S_T = 0, m_z = 0\rangle$), and correspond to the spin excitations of the many-body topological edge modes. This transition (I) is visible only when the tip is positioned at either end of the chain (S_1 or S_6). Since all spins have almost zero polarization in state $|4\rangle$, this shows that the spin distributions of the ground state $|1\rangle$ is mainly localized on the two end spins. Its frequency shifts linearly with increasing B_{tip}, providing clear evidence of the spin polarization of the topological edge states.

The topological phase exhibits a nearly fourfold degenerate ground state consisting of one singlet and three triplet states (Fig. 1d). We are able to extract the singlet–triplet splitting Δ_{st} by measuring the ESR transitions (Fig. 2b,e, transitions I and II). The splitting Δ_{st} is about 93 MHz, which gives a quantitative estimation of the effective coupling between the two observed edge modes[22]. It far exceeds the coupling for two isolated spins at this distance (<1 MHz), thus demonstrating the many-body nature of the topological modes.

To visualize the spatial distribution of the topological edge modes, we measured the ESR spectra along the spin chain as indicated by the dashed line in Fig. 2a, as well as its magnetic resonance imaging (Extended Data Fig. 1)[29]. The ESR mapping in Fig. 2c clearly reveals the localization of the spin distribution to the edges of the chain in the ground state $|1\rangle$. The strong spatial localization of the topological modes is reflected in the exponential decay of the local magnetization from the edge to the bulk, as shown in the calculated local average magnetization $\langle S_n^z \rangle$ on each site using the ground state $|1\rangle$ and the excited state $|4\rangle$ (Fig. 2d).

For comparison, we also constructed a dimerized 6-spin chain with the trivial configuration ($\delta < 0$) (Fig. 2f). Its ground state is a spin singlet, corresponding to a valence-bond solid configuration (Fig. 1e). In contrast to the strongly localized ESR transitions for the topological configuration, ESR spectra and mapping on the trivial one display almost uniform spatial distribution along the chain (Fig. 2g,h), indicating the absence of topological edge modes. Note that the difference between the topological and trivial nature of dimerized spin chains depends on the relative coupling strength between spins in the same unit cell and different unit cells[30].

In addition to these strong ESR peaks localized at the end spins, several weaker ESR peaks are also visible on all spins in the chains (Fig. 2b,g). These peaks correspond to transitions between other many-body states (as indicated in Fig. 2b,g), providing rich information about the excited states of the dimerized spin chains. The evolution of these additional ESR transitions agrees well with our theoretical simulations (Supplementary Section 2). This suggests that our theory describes well of the dimerized spin chains, further supporting the topological nature of the observed edge modes.

https://doi.org/10.1038/s41565-024-01775-2

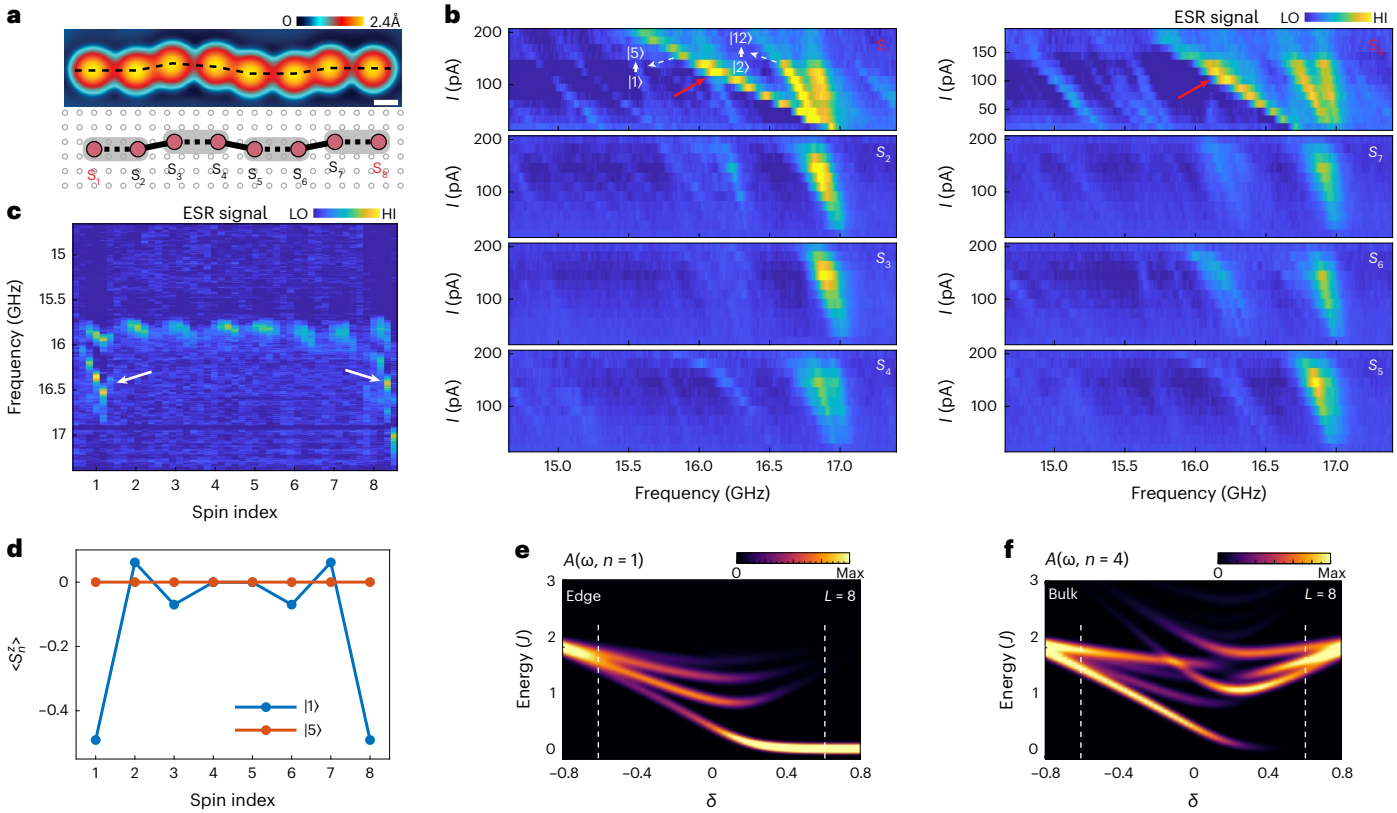

Fig. 3 | Topological edge states of an 8-spin chain. a, STM image (1.5 nm × 7 nm) and binding sites of a dimerized 8-spin chain on MgO with topological configuration. Scale bar, 5 Å. **b**, ESR spectra measured on each of the eight spins as a function of setpoint current I, which is approximately proportional to B_{tip} (V_{DC} = 50 mV, I = 20–200 pA, V_{RF} = 9–29 mV, B_{ext} = 0.67 T). The red arrows indicate the edge modes. The initial and final states of ESR transitions are labelled. In the colour bar, LO and HI mean the lowest and highest ESR signals. **c**, ESR spectra measured along the dashed line in **a** (V_{DC} = 50 mV, I = 120 pA, V_{RF} = 22 mV, B_{ext} = 0.61 T). The white arrows indicate the edge modes. **d**, Calculated average magnetization $\langle S_n^z \rangle$ for its ground state $|1\rangle$ and excited state $|5\rangle$. **e**,**f**, Evolution of the spin spectral function $A(\omega, n)$ as a function of δ. For $\delta > 0$, a zero-energy edge mode appears (**e**) and bulk spectral gap opens (**f**). The dashed lines indicate $\delta = \pm 0.61$ for the spin chains constructed.

Taking advantage of the atomic localization of the STM tunnelling current, we have also demonstrated the robustness of the topological end modes against local electron scattering (Extended Data Fig. 2). The quantum coherence time T_2 of the topological end modes of the dimerized chain is longer than isolated Ti spins[31], since the topological end mode is more delocalized and, therefore, local decoherence due to the tunnelling electrons is less effective.

We further compare the topological and trivial configurations of the dimerized spin model by increasing the number of atomic spins to eight (Fig. 3 and Extended Data Fig. 3). With increasing number of atoms, the low-energy singlet and triplet states are expected to get closer in energy, which becomes too small to resolve in the 8-spin chain, suggesting a fourfold topological degeneracy of the many-body ground state for sufficiently large chains. The local average magnetization $\langle S_n^z \rangle$ should decay exponentially with n for an infinite spin chain. For the topological configuration of the 8-spin chain, both the atomic-scale ESR spectra and ESR mapping exhibit localized ESR transitions at the two end spins (Fig. 3b,c), which agree well with the calculated $\langle S_n^z \rangle$ (Fig. 3d). We also calculated many-body spin spectral function as a function of the dimerization constant δ, which indicates the emergence of edge modes for $\delta > 0$ (Fig. 3e,f). The spectral function provides a model of the observed excitations.

Topological origin of edge spin modes

The topological invariant of the original interacting dimerized spin Hamiltonian $[H = J(1-\delta)\sum_n^{L/2} \mathbf{S}_{2n-1} \cdot \mathbf{S}_{2n} + J(1+\delta)\sum_n^{L/2-1} \mathbf{S}_{2n} \cdot \mathbf{S}_{2n+1}]$ can be calculated through a many-body generalization of the Zak phase[32] (Supplementary Section 1.3). We define the local topological order at a specific link $\langle ij \rangle$ by modifying the exchange couplings with a local $SU(2)$ spin rotation with angle θ as $J_{nm}\mathbf{S}_n \cdot \mathbf{S}_m \rightarrow J_{nm}\left[\frac{1}{2}\left(e^{-i\theta}S_n^+ S_m^- + e^{i\theta}S_n^- S_m^+\right) + S_n^z S_m^z\right]$, which results in a parameter-dependent Hamiltonian $H(\theta)$ and its associated ground state $|\mathrm{GS}(\theta)\rangle$. The Zak phase is then defined as $\gamma = i\oint_0^{2\pi} \left\langle \mathrm{GS}(\theta) \right| \frac{\partial}{\partial\theta} \left| \mathrm{GS}(\theta) \right\rangle \mathrm{d}\theta$. The dimerized Hamiltonian hosts a non-trivial Zak phase $\gamma = \pi$ for $\delta > 0$, giving rise to the observed topological edge modes; whereas the trivial phase corresponds to $\gamma = 0$ ($\delta < 0$). The dimerized Hamiltonian can also be adiabatically transformed to an XY spin model with nearest-neighbour exchange, which can be mapped via a Jordan–Wigner transformation to a dimerized fractional pseudo-fermion model with non-trivial Zak phase (Supplementary Section 1.2).

The dimerized Heisenberg model belongs to the same topological phase as the Haldane phase[24,26,27]. Similar to the Haldane phase[33], the topological edge modes in the dimerized spin chains are protected by the time-reversal symmetry in the original Hamiltonian (Supplementary Section 1.4). The time-reversal symmetry protects the quantization of the Zak phase. Under time-reversal symmetry, bilinear terms are invariant in the Hamiltonian and, thus, the topological modes are robust against second-nearest-neighbour interaction and disorder of the exchange couplings (Supplementary Sections 1.6 and 1.7). This makes the many-body topological Heisenberg model much more robust to lattice imperfections and fundamentally different from single-particle SSH model, which in realistic scenarios are not protected

https://doi.org/10.1038/s41565-024-01775-2

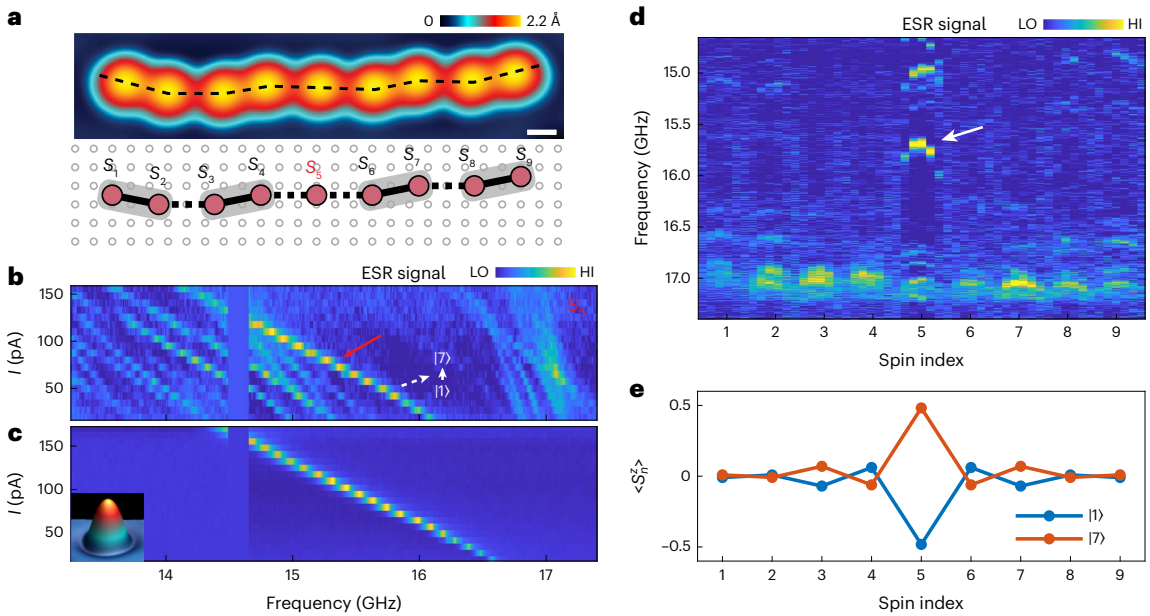

Fig. 4 | Topological bound mode of a 9-spin chain. a, STM image (1.75 nm × 8.3 nm) and binding sites of a dimerized 9-spin chain on MgO with a topological defect in the middle. Scale bar, 5 Å. **b**, ESR spectra measured on the middle spin as a function of setpoint current I, which is approximately proportional to B_{tip} (V_{DC} = 50 mV, I = 20–155 pA, V_{RF} = 6–30 mV, B_{ext} = 0.68 T). The red arrow indicates the bound mode. In the colour bar, LO and HI mean the lowest and highest ESR signals. **c**, ESR spectra measured on a single Ti spin (V_{DC} = 50 mV, I = 20–170 pA, V_{RF} = 6–30 mV). The stripes near 14.5 GHz are due to the uncompensated frequency-dependent RF transmission. Inset: STM image of the single Ti atom. **d**, ESR spectra measured along the dashed line in **a** (V_{DC} = 50 mV, I = 50 pA, V_{RF} = 20 mV). The white arrow indicates the bound mode. **e**, The calculated average magnetization $\langle S_n^z \rangle$ for its ground state $|1\rangle$ and excited state $|7\rangle$.

(Supplementary Section 1.11). We have further demonstrated the robustness of the fourfold degeneracy of many-body topological modes against long-range couplings by resolving a smaller splitting of the singlet and triplet ground states in a dimerized 6-spin chain with second-nearest-neighbour coupling (Extended Data Fig. 4). Under external magnetic field, the topological degeneracy is lifted, and the zero-energy topological edge states acquire a finite Zeeman energy (Supplementary Section 1.5). Note that the many-body spin wavefunctions are not altered by external magnetic field since the Zeeman term due to B_{ext} commutes with the dimerized Heisenberg interaction terms.

Topological defect in a dimerized 9-spin chain

In addition to dimerized spin chains with topological edge states as shown above, we also fabricated a dimerized 9-spin chain with a topological defect in the middle between two different dimer configurations (Fig. 4a and Extended Data Fig. 5). Since we have shown that dimerized spin chains with an even number of atoms have two topologically distinct phases, this odd-number dimerized spin chain should host a topological bound mode in the middle of chain because the left and right parts have different Zak phases. The topological nature of the mode stems from the robustness of the bound state excitation to the coupling to the left and right chains. Indeed, we observed an additional strong ESR transition only on the middle spin (as indicated by the red arrow in Fig. 4b). With increasing B_{tip}, the frequency of this ESR peak shifts with a similar rate as the ESR peak measured on an isolated Ti spin (Fig. 4c). This suggests that the local spin polarization of the topological mode is similar to the isolated spin, which agrees well with our theoretical calculation of the local average magnetization $\langle S_n^z \rangle$ (Fig. 4e). The spin-1/2 topological defect can also be clearly recognized in the ESR mapping in Fig. 4d.

Higher-order topological quantum magnet

We now move to the 2D spin lattice featuring higher-order topological modes, which has not been implemented in other artificial systems. Similar to the higher-order topological insulator with topological states emerging in two dimensions lower than the bulk[34,35], the 2D dimerized spin lattice we built exhibits many-body zero-dimensional spin excitations. Figure 5a shows a 2D dimerized 4 × 4 spin lattice, which can be viewed as a many-body generalization of a second-order topological insulator. The ESR spectra measured on the four corner spins show clear topological modes that appear as the strongest ESR excitation (Fig. 5b, red arrows). In contrast, the localized spin mode is absent at the edge or inner spins of the lattice (Extended Data Fig. 6). Importantly, we are able to obtain the effective coupling (~1 GHz) between the four topological corner modes by measuring the ESR transitions within the low-energy spin multiplets states (transitions I and II in Fig. 5c and Extended Data Fig. 6), highlighting their many-body nature. In addition, the ESR spectra along the outer spins of the square lattice again reveals the localization nature of the corner modes (Fig. 5d). Note that the weaker or relatively broadened ESR peaks on S_4 may result from a reduced quantum coherence time due to a fluctuating spin nearby.

The topological origin of the many-body corner modes can be understood by employing an auxiliary parton pseudo-fermionic representation of the original dimerized spin Hamiltonian (Supplementary Section 1.10). The emergence of topological modes can be observed by computing the parton spectral function $D(\omega, n)$. As shown in Fig. 5e, in-gap excitations appear for $\delta > 0$ at the corner of the lattice, which corresponds to the topological regime of the model. These corner modes coexist with a gap in bulk of the lattice (Fig. 5f), and in the thermodynamic limit lead to a 16-fold topological degeneracy of the ground state.

In contrast to the single-particle corner states of second-order topological insulators, which are protected by crystalline symmetries, the many-body topological corner modes of the spin lattice are protected by time-reversal symmetry, and thus they are robust to lattice imperfections such as third-nearest-neighbour exchange or breaking of crystalline symmetries (Supplementary Section 1.11).

Finally, we consider the difference between the topological edge or corner modes and an isolated spin-1/2. We fabricated dimerized 6-spin chains with varied coupling between the end and the bulk spins

https://doi.org/10.1038/s41565-024-01775-2

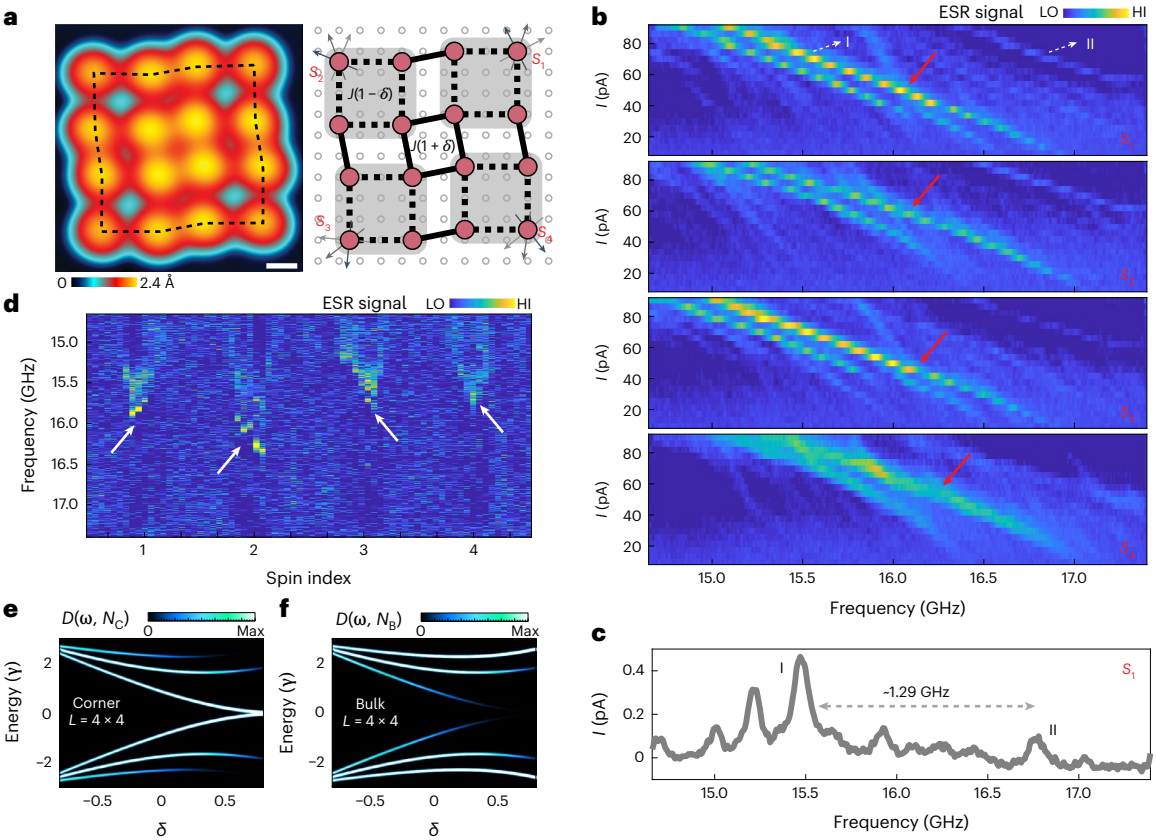

Fig. 5 | Higher-order topological mode of a 4 × 4 spin lattice. a, STM image (4 nm × 4 nm) and binding sites of a 4 × 4 spin lattice. Scale bar, 5 Å. **b**, ESR spectra measured on the corner spins (S_1, S_2, S_3, S_4) as a function of setpoint current I, which is approximately proportional to B_{tip} (V_{DC} = 50 mV, I = 10–90 pA, V_{RF} = 12–32 mV, B_{ext} = 0.77 T). The red arrows indicate the corner modes. In the colour bar, LO and HI mean the lowest and highest ESR signals. **c**, ESR spectrum showing transitions I and II, the frequency difference of which gives the effective coupling of the four corner modes (V_{DC} = 50 mV, I = 74 pA, V_{RF} = 16 mV). **d**, ESR spectra measured along the dashed line indicated in **a** (V_{DC} = 50 mV, I = 32 pA, V_{RF} = 26 mV). The white arrows indicate the corner modes. **e**,**f**, Parton spectral function of the 4 × 4 spin lattice at the corner (**e**) and the bulk (**f**). For $\delta > 0$, a corner mode appears whereas the bulk remains gapped.

(Extended Data Fig. 7). The ESR spectra measured at the end spins all give spin-1/2 modes, but the effective edge-mode coupling as well as the relative ESR amplitudes of other many-body spin transitions present in the intact dimerized spin chain decrease with reduced end–bulk coupling. This indicates that the topological edge mode transforms into a conventional decoupled spin-1/2 when the end–bulk coupling becomes vanishingly small. We further show how the topological edge or corner modes transform into decoupled excitations by calculating the spin spectral functions of the edge or corner and its neighbouring sites (Supplementary Sections 1.8 and 1.12).

Conclusions

Our work shows that many-body topological quantum states can be realized with spin-1/2 centres with carefully designed topology[24]. The insulating MgO layer allows us to demonstrate the intrinsic properties of the topological modes such as the robustness of the topological modes against local perturbations as well as long-range coupling. In addition, we are able to directly access the nearly degenerate singlet and triplet states with ESR–STM, which indicates the fourfold degeneracy of topological phase of the dimerized spin chains in the thermaldynamic limit. In combination with pump–probe electronic pulses[36,37], the atomically engineered quantum magnets provide the exciting opportunity to coherently manipulate the topological modes in the future. Our results establish a proof-of-concept demonstration of the potential of engineered spin lattices for realizing quantum spin liquid phases and topological order[38]. Ultimately, extending the size of the spin structures and introducing other degrees of freedom, such as superconductivity, would allow the exploration of exotic phases combining quantum magnetism and Yu–Shiba–Rusinov lattices[18].

Online content

Any methods, additional references, Nature Portfolio reporting summaries, source data, extended data, supplementary information, acknowledgements, peer review information; details of author contributions and competing interests; and statements of data and code availability are available at https://doi.org/10.1038/s41565-024-01775-2.

References

1. Narang, P., Garcia, C. A. C. & Felser, C. The topology of electronic band structures. *Nat. Mater.* **20**, 293–300 (2021).
2. Tokura, Y., Yasuda, K. & Tsukazaki, A. Magnetic topological insulators. *Nat. Rev. Phys.* **1**, 126–143 (2019).
3. Kiczynski, M. et al. Engineering topological states in atom-based semiconductor quantum dots. *Nature* **606**, 694–699 (2022).
4. de Léséleuc, S. et al. Observation of a symmetry-protected topological phase of interacting bosons with Rydberg atoms. *Science* **365**, 775–780 (2019).
5. Sompet, P. et al. Realizing the symmetry-protected Haldane phase in Fermi–Hubbard ladders. *Nature* **606**, 484–488 (2022).
6. Drost, R., Ojanen, T., Harju, A. & Liljeroth, P. Topological states in engineered atomic lattices. *Nat. Phys.* **13**, 668–671 (2017).
7. Mishra, S. et al. Observation of fractional edge excitations in nanographene spin chains. *Nature* **598**, 287–292 (2021).

8. Kempkes, S. N. et al. Robust zero-energy modes in an electronic higher-order topological insulator. *Nat. Mater.* **18**, 1292–1297 (2019).
9. Meier, E. J., An, F. A. & Gadway, B. Observation of the topological soliton state in the Su–Schrieffer–Heeger model. *Nat. Commun.* **7**, 13986 (2016).
10. St-Jean, P. et al. Lasing in topological edge states of a one-dimensional lattice. *Nat. Photon.* **11**, 651–656 (2017).
11. Rizzo, D. J. et al. Topological band engineering of graphene nanoribbons. *Nature* **560**, 204–208 (2018).
12. Gröning, O. et al. Engineering of robust topological quantum phases in graphene nanoribbons. *Nature* **560**, 209–213 (2018).
13. Schneider, L. et al. Topological Shiba bands in artificial spin chains on superconductors. *Nat. Phys.* **17**, 943–948 (2021).
14. Khajetoorians, A. A., Wegner, D., Otte, A. F. & Swart, I. Creating designer quantum states of matter atom-by-atom. *Nat. Rev. Phys.* **1**, 703–715 (2019).
15. Choi, D.-J. et al. Colloquium: atomic spin chains on surfaces. *Rev. Mod. Phys.* **91**, 041001 (2019).
16. Nadj-Perge, S. et al. Observation of Majorana fermions in ferromagnetic atomic chains on a superconductor. *Science* **346**, 602–607 (2014).
17. Liebhaber, E. et al. Quantum spins and hybridization in artificially-constructed chains of magnetic adatoms on a superconductor. *Nat. Commun.* **13**, 2160 (2022).
18. Soldini, M. O. et al. Two-dimensional Shiba lattices as a possible platform for crystalline topological superconductivity. *Nat. Phys.* **19**, 1848–1854 (2023).
19. Yang, K. et al. Probing resonating valence bond states in artificial quantum magnets. *Nat. Commun.* **12**, 993 (2021).
20. Zhao, Y. et al. Quantum nanomagnets in on-surface metal-free porphyrin chains. *Nat. Chem.* **15**, 53–60 (2023).
21. Zhao, C. et al. Tunable topological phases in nanographene-based spin-1/2 alternating-exchange Heisenberg chains. Preprint at https://arxiv.org/abs/2402.13590v1 (2024).
22. Yang, K. et al. Engineering the eigenstates of coupled spin-1/2 atoms on a surface. *Phys. Rev. Lett.* **119**, 227206 (2017).
23. Bae, Y. et al. Enhanced quantum coherence in exchange coupled spins via singlet–triplet transitions. *Sci. Adv.* **4**, eaau4159 (2018).
24. Hida, K. Crossover between the Haldane-gap phase and the dimer phase in the spin-1/2 alternating Heisenberg chain. *Phys. Rev. B* **45**, 2207–2212 (1992).
25. Yang, K. et al. Tuning the exchange bias on a single atom from 1 mT to 10 T. *Phys. Rev. Lett.* **122**, 227203 (2019).
26. Haghshenas, R., Langari, A. & Rezakhani, A. T. Symmetry fractionalization: symmetry-protected topological phases of the bond-alternating spin-1/2 Heisenberg chain. *J. Phys. Condens. Matter* **26**, 456001 (2014).
27. Luo, Q., Zhao, J., Wang, X. & Kee, H.-Y. Unveiling the phase diagram of a bond-alternating spin-1/2 *K*–Γ chain. *Phys. Rev. B* **103**, 144423 (2021).
28. Lado, J. L., Ortiz, R. & Fernández-Rossier, J. in *Graphene Nanoribbons* (eds. Brey, L., Seneor, P. & Tejeda, A.) Ch. 4 (IOP Publishing, 2019).
29. Willke, P. et al. Magnetic resonance imaging of single atoms on a surface. *Nat. Phys.* **15**, 1005–1010 (2019).
30. Benalcazar, W. A., Bernevig, B. A. & Hughes, T. L. Electric multipole moments, topological multipole moment pumping, and chiral hinge states in crystalline insulators. *Phys. Rev. B* **96**, 245115 (2017).
31. Willke, P. et al. Probing quantum coherence in single-atom electron spin resonance. *Sci. Adv.* **4**, eaaq1543 (2018).
32. Hatsugai, Y. Quantized Berry phases for a local characterization of spin liquids in frustrated spin systems. *J. Phys. Condens. Matter* **19**, 145209 (2007).
33. Pollmann, F., Turner, A. M., Berg, E. & Oshikawa, M. Entanglement spectrum of a topological phase in one dimension. *Phys. Rev. B* **81**, 064439 (2010).
34. Noh, J. et al. Topological protection of photonic mid-gap defect modes. *Nat. Photon.* **12**, 408–415 (2018).
35. Schindler, F. et al. Higher-order topology in bismuth. *Nat. Phys.* **14**, 918–924 (2018).
36. Yang, K. et al. Coherent spin manipulation of individual atoms on a surface. *Science* **366**, 509–512 (2019).
37. Wang, Y. et al. An atomic-scale multi-qubit platform. *Science* **382**, 87–92 (2023).
38. Broholm, C. et al. Quantum spin liquids. *Science* **367**, eaay0668 (2020).

Methods

Sample preparation

Measurements were performed in a low-temperature STM (Unisoku USM1300) with home-built radio frequency (RF) components for ESR measurement. MgO is two MLs thick and was grown on Ag(001) single crystal by thermally evaporating Mg in an ~10^{-6} Torr O_2 environment[39]. Ti and Fe atoms were deposited from pure metal rods by e-beam evaporation onto the sample held at ~10 K. An external magnetic field (0.59 T to 0.77 T as indicated in the figure captions) was applied at ~8° off the surface. STM images were acquired in constant-current mode, and all voltages refer to the sample voltage with respect to the tip.

Spin-polarized tip

The Pt–Ir STM tip was coated with silver by indentations into the Ag sample until the tip gave a good lateral resolution in the STM image. To prepare a spin-polarized tip, approximately one to five Fe atoms were each transferred from the MgO onto the tip by applying a bias voltage (~0.55 V) while withdrawing the tip from near point contact with the Fe atom. The degree of spin polarization was verified by the asymmetry in dI/dV spectra of Ti with respect to voltage polarity.

RF measurement

The continuous wave ESR spectra were acquired by sweeping the frequency of an RF voltage V_{RF} generated by the RF generator (Agilent E8257D) across the tunnelling junction and monitoring changes in the tunnelling current. The current signal was modulated at 95 Hz by chopping V_{RF}, which allowed readout of the current by a lock-in technique[39]. The RF and direct current (DC) voltages were combined at room temperature using an RF diplexer, and guided to the STM tip through semi-rigid coaxial cables with a loss of ~30 dB at 20 GHz.

Data availability

The data that support the plots within this paper are available via the Figshare repository at https://doi.org/10.6084/m9.figshare.26379964. Additional data are available from the authors upon request.

References

39. Baumann, S. et al. Electron paramagnetic resonance of individual atoms on a surface. *Science* **350**, 417–420 (2015).

Acknowledgements

This work is supported by the National Key R&D Program of China (2022YFA1204100 (K.Y. and L.J.)), the Beijing Natural Science Foundation (Z230005 (K.Y., and P.F.)), the National Natural Science Foundation of China (12174433 (K.Y.), 52272170 (L.J.) and 62488201 (H.-J.G.)), and the CAS Project for Young Scientists in Basic Research (YSBR-003 (K.Y.)). J.L.L. acknowledges the computational resources provided by the Aalto Science-IT project, the financial support from the Academy of Finland Projects (nos. 331342 and 358088) and the Jane and Aatos Erkko Foundation.

Author contributions

K.Y. and J.L.L. designed the experiment. H.W., P.F., J.C., L.J. and K.Y. carried out the STM measurements. J.L.L. developed the theoretical model. H.W., L.J., H.-J.G., K.Y. and J.L.L. performed the analysis and wrote the manuscript with help from all authors. All authors discussed the results and edited the manuscript.

Competing interests

The authors declare no competing interests.

Additional information

Extended data is available for this paper at https://doi.org/10.1038/s41565-024-01775-2.

Supplementary information The online version contains supplementary material available at https://doi.org/10.1038/s41565-024-01775-2.

Correspondence and requests for materials should be addressed to Jose L. Lado or Kai Yang.

Peer review information *Nature Nanotechnology* thanks Dario Bercioux, Rémy Pawlak and the other, anonymous, reviewer for their contribution to the peer review of this work.

https://doi.org/10.1038/s41565-024-01775-2

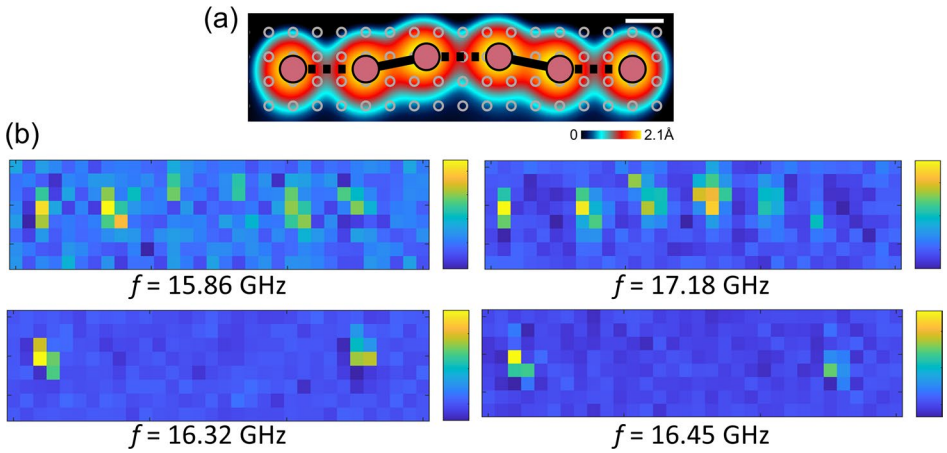

Extended Data Fig. 1 | Magnetic resonance imaging (MRI) of the dimerized 6-spin chain. (**a**) STM image (1.3 nm × 5.6 nm) and binding sites for the dimerized 6-spin chain with topological configuration. Scale bar: 5 Å. (**b**) MRI of the chain showing spatially resolved spin resonance signal for a fixed frequency at f = 15.86, 17.18, 16.32 and 16.45 GHz, respectively (V_{DC} = 50 mV, I = 50 pA, V_{RF} = 16 mV, B_{ext} = 0.68 T).

https://doi.org/10.1038/s41565-024-01775-2

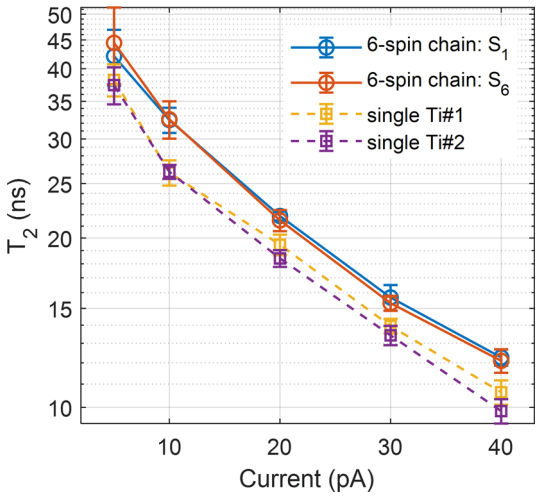

Extended Data Fig. 2 | Quantum coherence T_2 of the end modes of a dimerized 6-spin chain and isolated Ti spins. T_2 was obtained by measuring the linewidth of the ESR peak at different V_{RF} (V_{DC} = 50 mV, I = 5–40 pA, V_{RF} = 6–55 mV, B_{ext} = 0.68 T). Error bars are from the fitting uncertainties of T_2 with a 95% confidence.

https://doi.org/10.1038/s41565-024-01775-2

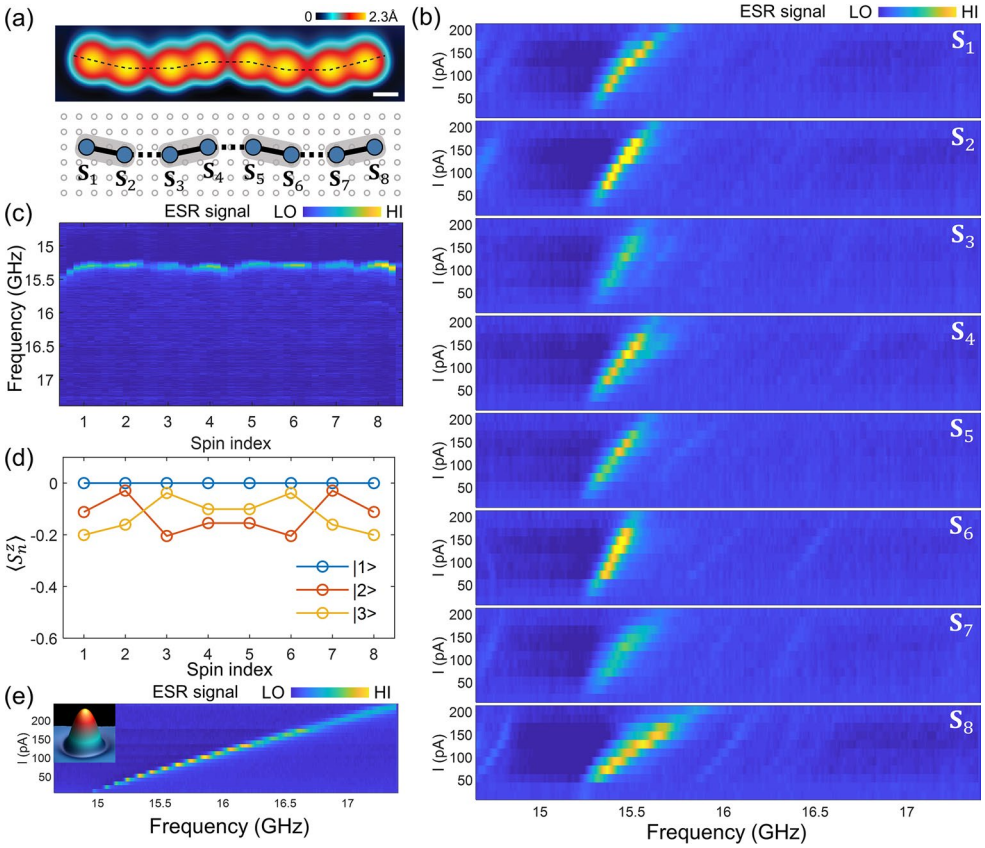

Extended Data Fig. 3 | An 8-spin chain with topologically trivial configuration. (**a**) STM image (1.5 nm × 7 nm) and binding sites of a dimerized 8-spin chain on MgO. Scale bar: 5 Å. (**b**) ESR spectra measured on each of the 8 spins as a function of setpoint current I, which is approximately proportional to B_{tip} (V_{DC} = 50 mV, I = 20–220 pA, V_{RF} = 4–25 mV, B_{ext} = 0.59 T). (**c**) ESR spectra measured along the dashed line in a (V_{DC} = 50 mV, I = 60 pA, V_{RF} = 20 mV). (**d**) Calculated average magnetization $\langle S_n^z \rangle$ for its ground state $|1\rangle$ and two excited states $|2\rangle$ and $|3\rangle$. (**e**) ESR spectra measured on a single Ti spin (V_{DC} = 50 mV, I = 10–240 pA, V_{RF} = 4–25 mV).

https://doi.org/10.1038/s41565-024-01775-2

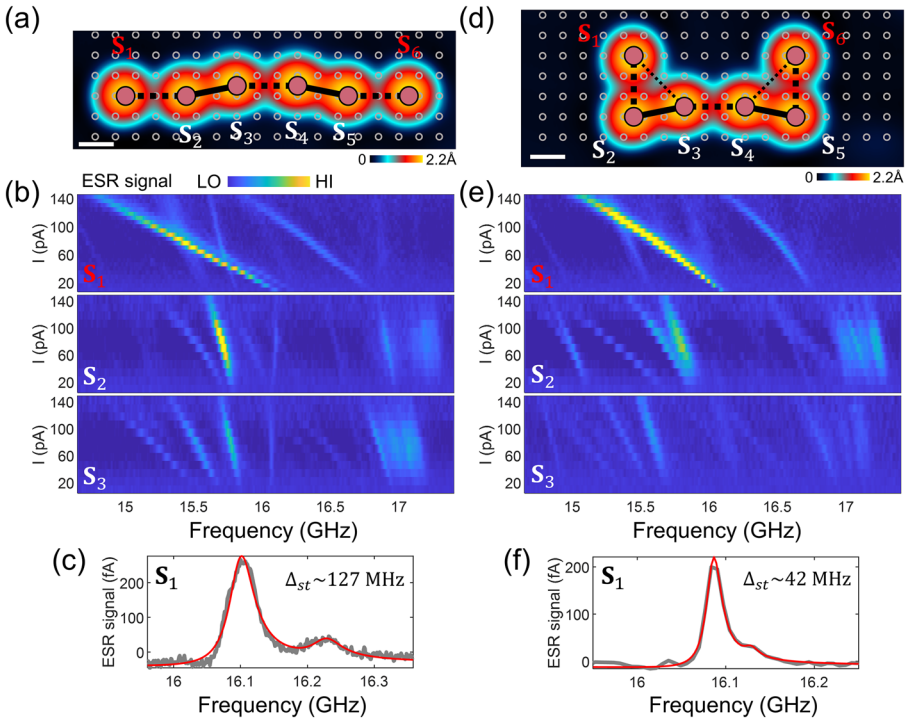

Extended Data Fig. 4 | Dimerized 6-spin chains without and with the second-nearest-neighbor coupling. STM images and ESR spectra of dimerized 6-spin chains without (**a**–**c**) and with (**d**–**f**) second-nearest-neighbor coupling (-1 GHz). Scale bars in (**a**, **d**): 5 Å. For the spin chain in (**d**), the second-nearest-neighbor coupling is between S_1 and S_3 as well as between S_4 and S_6. (**b**, **e**) ESR spectra measured on spins S_1, S_2 and S_3 as a function of setpoint current I, which is approximately proportional to B_{tip} (V_{DC} = 50 mV, I = 10–142 pA, V_{RF} = 2.5–10 mV, B_{ext} = 0.68 T). (**c**, **f**) Zoom-in ESR spectra showing the singlet-triplet splitting (V_{DC} = 50 mV, I = 10 pA, V_{RF} = 10-20 mV).

https://doi.org/10.1038/s41565-024-01775-2

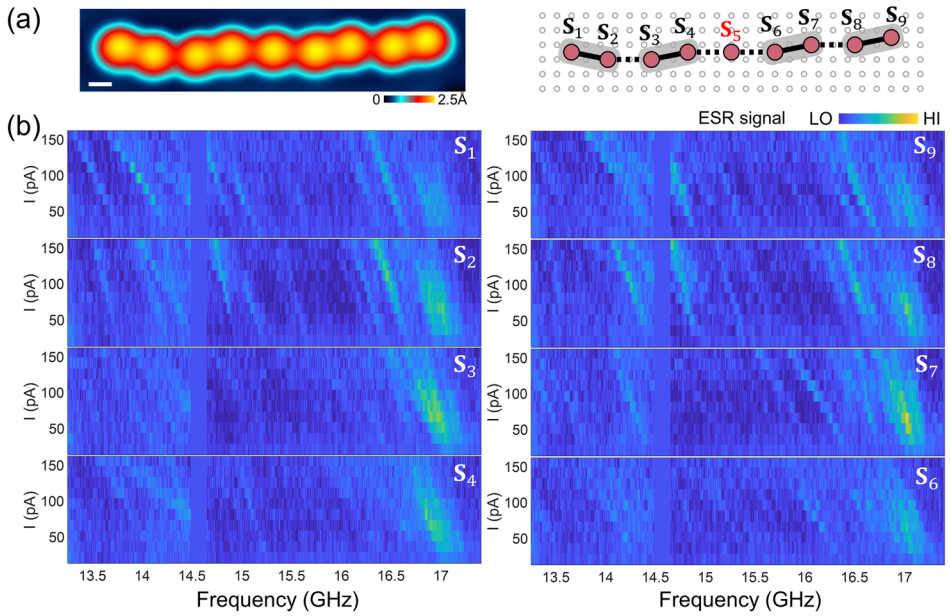

Extended Data Fig. 5 | ESR spectra of S_1 to S_4 and S_6 to S_9 of the 9-spin chain. (**a**) STM image (1.75 nm × 8.3 nm) and binding sites of the dimerized 9-spin chain on MgO with a topological defect in the middle. Scale bar: 5 Å. (**b**) ESR spectra measured on each of the 8 spins as a function of setpoint current I, which is approximately proportional to B_{tip} (V_{DC} = 50 mV, I = 20–155 pA, V_{RF} = 6–30 mV, B_{ext} = 0.68 T).

https://doi.org/10.1038/s41565-024-01775-2

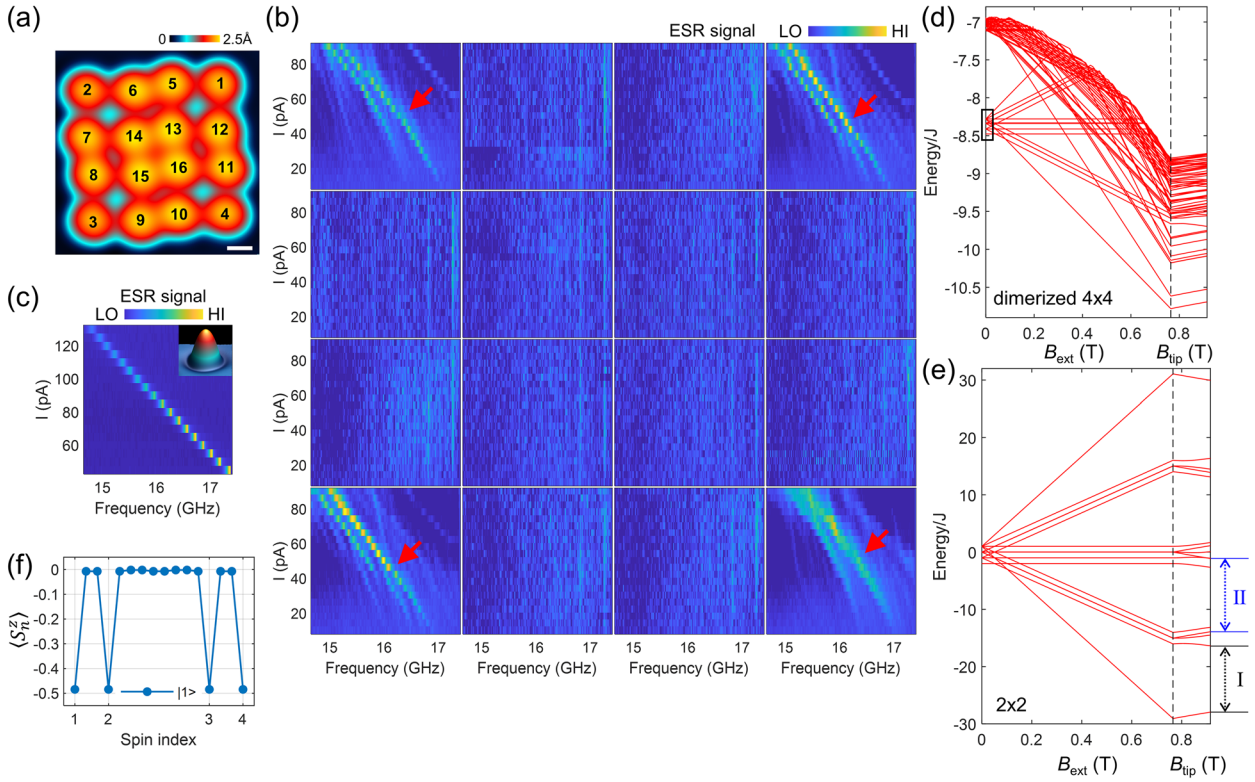

Extended Data Fig. 6 | ESR spectra of all the spins of the dimerized 4×4 spin lattice. (**a**) STM image (4 nm × 4 nm) of the 4×4 spin lattice. Scale bar: 5 Å. (**b**) ESR spectra measured on each of the 16 spins as a function of setpoint current I, which is approximately proportional to B_{tip} (V_{DC} = 50 mV, I = 10–90 pA, V_{RF} = 12–32 mV, B_{ext} = 0.77 T). Red arrows indicate the corner modes. (**c**) ESR spectra measured on a single Ti spin (V_{DC} = 50 mV, I = 40–125 pA, V_{RF} = 10–16 mV). (**d**) Energy level diagram showing the lowest 64 eigenenergies (as a function of B_{ext} and B_{tip}) of the dimerized 4×4 spin lattice. (**e**) Energy level diagram of a 2×2 spin lattice, which is approximate to the low-energy spectrum of the dimerized 4×4 spin lattice. (**f**) Calculated average magnetization $\langle S_n^z \rangle$ of different sites for the ground state $|1\rangle$.

https://doi.org/10.1038/s41565-024-01775-2

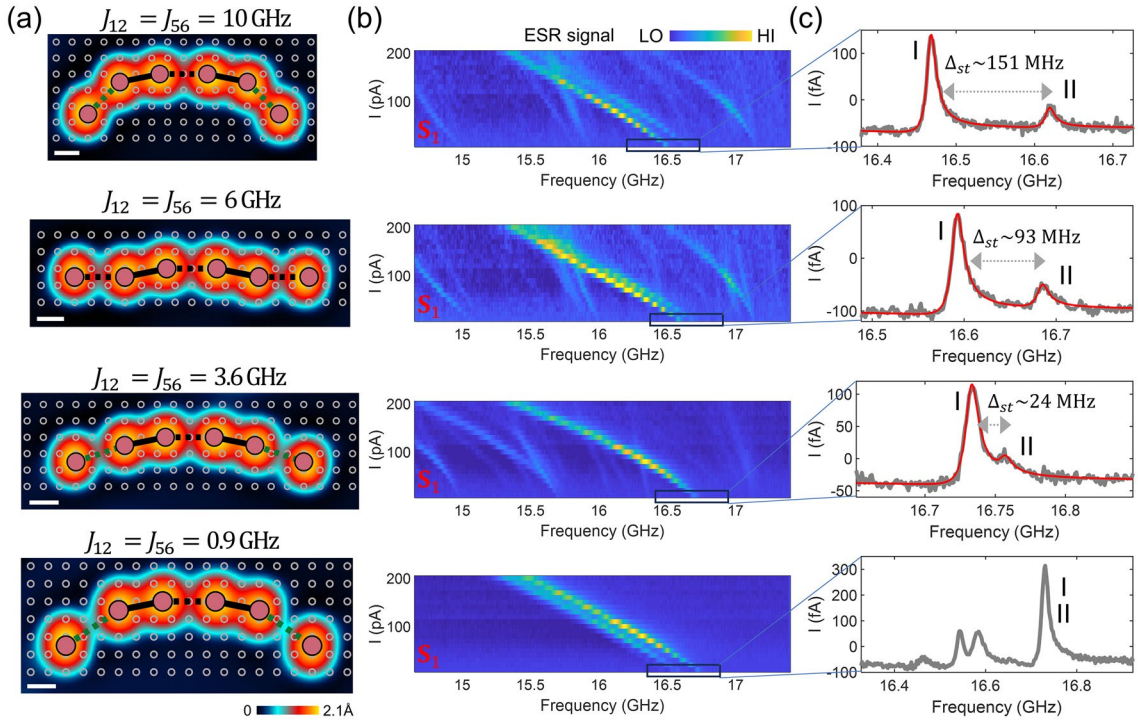

Extended Data Fig. 7 | Dimerized 6-spin chains with varied coupling between the end spins and the bulk spins. (**a**) STM image and binding sites for spin chains with $J_{\text{end-bulk}}$ = 10, 6, 3.6, 0.9 GHz, respectively. The bulk coupling is $J(1+\delta)/J(1-\delta)$ = 25/6 GHz. Scale bars: 5 Å. (**b**) ESR spectra measured on the end spins as a function of setpoint current I (V_{DC} = 50 mV, I = 10–200 pA, V_{RF} = 5–28 mV, B_{ext} = 0.68 T). (**c**) Zoom-in of the ESR spectra measured at low setpoint currents (V_{DC} = 50 mV, I = 5–10 pA, V_{RF} = 21–28 mV), showing transitions I and II, the frequency difference of which gives the singlet-triplet splittings.